Available online at www.sciencedirect.com

jmr&t
Journal of Materials Research and Technology

journal homepage: www.elsevier.com/locate/jmrt

Original Article

NdB_6 ceramic nanoparticles: First principles calculations, mechanochemical synthesis and strain engineering

Burçak Boztemur [a,b,**], *Mubashir Mansoor* [c,d], *Faruk Kaya* [d], *Mantao Huang* [e], *Emre Tekoğlu* [e], *M.Lütfi Öveçoğlu* [a], *Ju Li* [e,f], *Duygu Ağaoğulları* [a,b,*]

[a] *Istanbul Technical University, Faculty of Chemical and Metallurgical Engineering, Department of Metallurgical and Materials Engineering, Particulate Materials Laboratories (PML), Graphene and 2D Materials Laboratory, 34469 Maslak, Istanbul, Türkiye*

[b] *Istanbul Technical University, Prof. Dr. Adnan Tekin Materials Science and Production Technologies Applied Research Center (ATARC), 34469 Maslak, Istanbul, Türkiye*

[c] *Istanbul Technical University, Faculty of Science and Letters, Department of Applied Physics, 34469 Maslak, Istanbul, Türkiye*

[d] *Istanbul Technical University, Faculty of Chemical and Metallurgical Engineering, Department of Metallurgical and Materials Engineering, 34469 Maslak, Istanbul, Türkiye*

[e] *Department of Materials Science and Engineering, Massachusetts Institute of Technology, 77 Massachusetts Avenue, Cambridge, MA 02139, United States*

[f] *Department of Nuclear Science and Engineering, Massachusetts Institute of Technology, 77 Massachusetts Avenue, Cambridge, MA 02139, United States*

ARTICLE INFO

Article history:
Received 7 February 2023
Accepted 18 April 2023
Available online 25 April 2023

Keywords:
Nd boride powders
Strain engineering
Density functional theory
Defect structure
Superplasticity
CALPHAD

ABSTRACT

Borides are usually hard and brittle materials; however, we report the synthesis of superplastic nanostructured NdB_6 ceramic powders, counter to the conventional wisdom that borides are always brittle. We investigate that through strain engineering, NdB_6 can be made extremely ductile if the lattice is compressively strained and highly defected, based on transmission electron microscopy (TEM) and density functional theory (DFT) calculations. In this study, the synthesis conditions were designed based on CALPHAD modelling, and the superplastic NdB_6 powders were successfully obtained through mechanochemical synthesis (MCS) of Nd_2O_3, B_2O_3 and Mg initial materials in a high-energy ball mill. Following MCS, the powders were purified in a hydrochloric acid (HCl) containing aqueous solution in order to leach out MgO by-product. The purified powders were characterized using X-ray diffractometry (XRD), Helium (He) gas pycnometry, scanning electron microscopy (SEM) coupled with energy dispersive spectroscopy (EDS), transmission electron microscopy (TEM), particle size analysis (PSA) and magnetometry techniques, which demonstrated

Abbreviations: NdB6, neodymium hexaboride; NdB4, neodymium tetraboride; DFT, density functional theory; MCS, mechanochemical synthesis.

* Corresponding author.
** Corresponding author.
E-mail addresses: boztemur15@itu.edu.tr (B. Boztemur), bozkurtdu@itu.edu.tr (D. Ağaoğulları).

https://doi.org/10.1016/j.jmrt.2023.04.165

2238-7854/© 2023 The Author(s). Published by Elsevier B.V. This is an open access article under the CC BY-NC-ND license (http://creativecommons.org/licenses/by-nc-nd/4.0/).

NdB_6 nanoparticles with an average particle size of 118 nm belonging paramagnetic behavior at cryogenic temperatures. DFT calculations have been carried out through to investigate the structural, mechanical, electronic, optical, thermodynamic and magnetic properties of NdB_6. The impact of various defects was examined, which revealed the significance of boron vacancies and compressive strains in the superplastic form of NdB_6.
© 2023 The Author(s). Published by Elsevier B.V. This is an open access article under the CC BY-NC-ND license (http://creativecommons.org/licenses/by-nc-nd/4.0/).

1. Introduction

Metal borides are important and unique advanced ceramic materials utilized at high-temperature applications. Rare-earth (RE) borides are a family of high-temperature materials with extremely fascinating chemical and structural properties [1,2]. Thanks to the strong bonding of boron, great stability and high hardness in extreme conditions are observed for many boride materials. As a new development, exciting magnetic and electronic properties have been found in the newly discovered RE boron compounds, attributed to their metallic bonding component and contributions of the *f*-electrons [3,4].

The study of RE borides has attracted a lot of attention over the past three decades. Six distinct families have been discovered, namely: REB_2, REB_4, RE_2B_5, REB_6, REB_{12}, and REB_{66} [5]. Amongst the RE borides, RE hexaborides (REB_6) have attracted more attention thanks to their extreme characteristics such as low work function, high melting point, chemical stability, magnetic property and superconductivity [6–8]. These properties have also made REB_6 of considerable interest as field-emission sources in various devices. REB_6 are also used in high-energy optical systems, as sensors for high-resolution radiation detectors and as electrical coatings for resistors because of their low work function, small optical size, high brightness, low volatility at high temperatures, long service life, and the mono energetic character of their thermionic electron emissions [9–11]. Neodymium hexaboride (NdB_6) is an important member of REB_6 group materials, and has very interesting magnetic and mechanical properties, with one of the lowest work function amongst the REB_6 family [7,8]. According to the Nd–B binary phase diagram, Nd_2B_5, NdB_4, NdB_6 and NdB_{66} are the four phases in this binary system, with NdB_6 being the most stable high-temperature phase [12]. NdB_6 has a cubic structure with a space group of Pm-3m, in which Nd atoms are surrounded by six boron atom octahedra [13]. NdB_6 has low density (4.95 g/cm^3), high melting point (2610 °C), high thermal conductivity (47 $Wm^{-1}K^{-1}$) and low thermal expansion coefficient (7.3×10^{-6} °C^{-1}) [14–18]. NdB_6 orders in an A-type collinear antiferromagnetic structure below $T_N \approx 8$ K [19–22].

Neodymium hexaboride powders can be fabricated by using various synthesis methods. NdB_6 has been synthesized by boro/carbothermal synthesis method using carbon and boron carbide, combustion synthesis method, mechanochemical synthesis, flux-controlled self-catalyzed method and facile catalysis-free method [10,14,19,23,24]. For instance, NdB_6 powders were synthesized from Nd_2O_3–B_4C system under the conditions of 10^{-2} Pa vacuum and 4 h holding time at temperature above 1500 °C [13]. Ultra-fine NdB_6 powders were fabricated via combustion synthesis method starting from B_2O_3, Nd_2O_3 and Mg powder mixtures [23]. Pure NdB_6 nanocrystals were synthesized by mechanochemical alloying of Nd, B_2O_3 and Mg powders at room temperature with milling rate of 300 rpm for different durations up to 30 h and by subsequent CH_3COOH leaching [24]. NdB_6 were produced with a simple flux-controlled self-catalyzed method by using BCl_3 gas and Nd powders at 1000 °C [25]. Also, NdB_6 nanowires synthesized via a facile self-catalysis growth method using Nd powders and BCl_3/H_2 gas mixture [26]. Amorphous boron (99.99% purity) mixed with Nd_2O_3 were weighed in the ratio of B:Nd = 5:1, and reacted for 15 min in a high pressure assembler to yield boron-rich NdB_6 [27].

Borides are known for their hardness and brittle character, which significantly impairs their use in a wide range of engineering applications. However, there have been two recent theoretical predictions by Pan et al. [28] and Zhou et al. [29] which demonstrate tuning the anisotropic shear moduli, and formation of boron vacancy can lead to the formation of a ductile boride lattice. Therefore, in this study, we have aimed to produce nanostructured NdB_6 powders through an experimental set-up that can achieve the necessary requirements in terms of defect equilibria and shear moduli for making superplasticity possible. As mentioned, there are limited studies focused on the synthesis of NdB_6 powders in the literature up to now. In the reported studies, different neodymium and boron sources such as Nd, Nd_2O_3, B, B_2O_3, B_4C and BCl_3 were used for the preparation of NdB_6. However, the synthesis of NdB_6 powders has never been achieved through Nd_2O_3, B_2O_3 and Mg precursor blends by using the combination of MCS driven by high energy ball milling and leaching processes, which not only made the production of the hexaboride phase possible, but also facilitated the evolution of interesting defects within the synthesized nanostructures that lead to superplasticity. There is only one investigation focused on the MCS process in the present literature where a low speed milling (planetary ball mill at 300 rpm, for 15 h) and leaching (by CH_3COOH) processes were conducted on the Nd–B_2O_3–Mg powder mixtures [24]. However, given the cost and difficulties associated with the use of metallic Nd, and the importance of lattice strain in the appearance of superplasticity, the present study puts forth a cost-effective process for the production of the superplastic nanostructured NdB_6 powders thanks to the low-cost raw materials used and the facile method through simple equipment. The MCS method utilized in this study

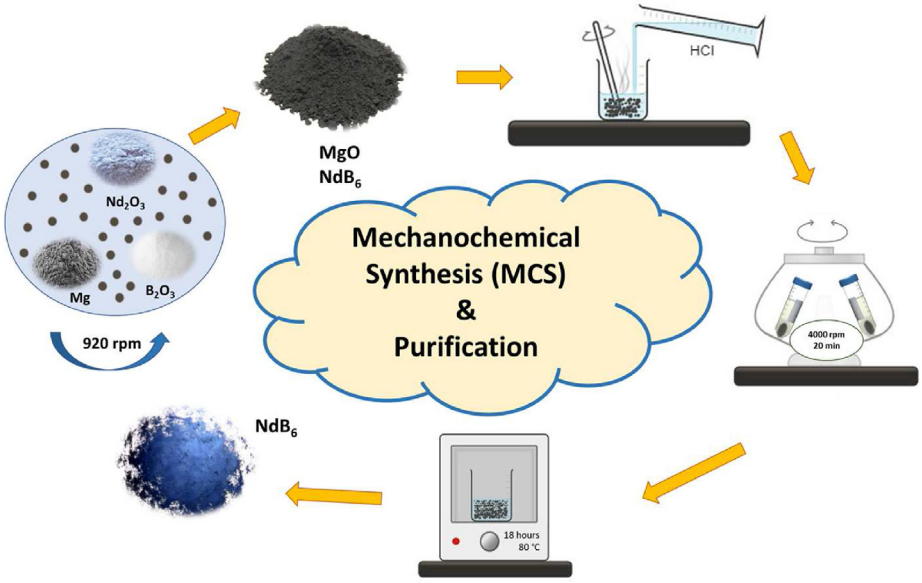

Fig. 1 – Schematic of synthesis procedure of NdB_6 powders.

offers several advantages to the conventional methods of nanoparticle synthesis, namely, the control on purity and particle size, absence of externally applied heat (accepted as room temperature process), versatile experimental set-up, ease of experimental procedure, and strict control over the chemical potentials in the system based on the environmental conditions and precursors that can be utilized [30–32]. This makes it possible to induce a wide range of chemically induced strains (through defect-assisted strain engineering) that ultimately determine the final material properties. Therefore, an experimental study combined with the CALPHAD and DFT modellings is put together for the first time on the superplastic nanostructured NdB_6 powders derived from MCS and acid leaching.

2. Experimental and computational methods

2.1. Raw materials and precursor preparation

Nd_2O_3 (Alfa Aesar, 99% pure), B_2O_3 (ETI Mine, 98% pure) and Mg powders (Alfa Aesar, 99.8% pure) were used as the starting materials. The average particle sizes of the Nd_2O_3, B_2O_3 and Mg initial powders were measured by using a Malvern Mastersizer 2000 particle size analyzer and determined as ~5 μm, 386 μm and 108 μm, respectively. Stoichiometry for the synthesis of NdB_6 from the Nd_2O_3, B_2O_3 and Mg powders is given by the reduction reaction in Eq. (1). The stoichiometric amounts of the initial reactants were Nd_2O_3: B_2O_3: Mg = 1.598 : 1.984: 2.424 g. The total powder batches of 6 g were mixed in a WAB T2C Turbula blender for 2 h with the aim of homogenization, and hereafter they are called as-blended powders. Thermochemical modelling studies were done by using FactSage 7.3 software [33] in order to simulate Eq. (1) with respect to varying B_2O_3 content ($0<A<10$ mol) at different temperatures (25 °C $<T<$ 800 °C). In the calculations, "equilib" module was used under 1 atm and non-adiabatic conditions ($\Delta H \neq 0$) since the experimental set up is not heat insulated, and the temperature of the system can rise up to 600 °C. FactPS and SGTE 2017 databases were selected for the gas, compound and solution phases.

$$Nd_2O_3 + 6\,B_2O_3 + 21\,Mg \rightarrow 2\,NdB_6 + 21\,MgO \quad (1)$$

2.2. Mechanochemical synthesis and purification

As-blended powders were sealed under Argon (Ar) atmosphere (Linde, 99.999% pure) in an MBraun glove box. For producing NdB_6, mechanochemical synthesis (MCS) was triggered by milling of the as-blended powders in a high energy Nano-MultiMix mill at 920 rpm for different durations up to 8 h. The required energy needed to initiate the reaction was provided by high energy collisions, induced into powder particles via mechanical deformation. The ball-to-powder weight ratio was fixed at 10:1. Hardened steel vial (50 ml) and hardened steel balls (6 mm diameter) were used as milling media. After MCS, selective acid leaching was applied for the removal of MgO by-product with 2 M, 4 M and 6 M hydrochloric acid (HCl, Merck, 37%) solution under ultrasonic stirring and heating using a Bandelin Sonorex RK-100H ultrasonic bath. The leaching treatment was conducted at 80 °C for 20 min with a solid-to-liquid ratio of 1 g/10 cm^3. The residue was then separated from the leaching solution by repeated centrifugation (Hettich Rotofix 32 A, 4000 rpm, 20 min), decantation and rinsing steps. The residue was dried in an FN 500 stove at 80 °C for 18 h in air. The residue is hereafter referred to as leached powders. The schematic of powder synthesis procedure is shown in Fig. 1.

2.3. Characterization

X-ray diffraction (XRD) investigations of the as-blended, mechanochemically synthesized (MCS'd) and leached

powders were performed using a Bruker D8 Advanced Series X-ray powder diffractometer, with CuK$_\alpha$ ($\lambda = 0.154$ nm, 35 kV and 40 mA) radiation in the 2θ range of 10–90° incremented at a step size of 0.02° at a rate of 2°/min. The International Center for Diffraction Data® (ICDD) powder diffraction files were utilized to determine the crystal structure and lattice parameter(s) of the crystalline phases. The average crystallite sizes of the MCS'd NdB_6 powders were measured by utilizing Bruker-AXS TOPAS V3.0 software based on the modified Scherrer's formula [34]. The amounts of the different phases in the MCS'd NdB_6 powders were identified by the semi-quantitative Rietveld refinement method based on the related XRD patterns. The density of the leached powders was measured using Micromeritics AccuPyc II 1340 gas pycnometer in an 1 cm^3 sample chamber at room temperature using He gas (Linde, 99.996% pure) as the displacement medium. Particle size analyses (PSA) were conducted for the leached powders using a Microtrac Nano-flex particle size analyzer equipped with a Bandelin Sonopuls ultrasonic homogenizer in alcohol media. Also, surfactants were not used for dispersion in this solution. A Thermo Scientific Quattro S equipment was used for scanning electron microscopy (SEM) and energy dispersive spectroscopy (EDS) analyses of the MCS'd and leached powders. EDS results were reported as the arithmetic means of three different measurements taken from the same regions in the samples. A JEOL JEM-ARM200CFEG UHR-TEM (equipped with STEM, Cs corrected STEM, EDS, Gatan Quantum GIF and Digital CCD Camera) was used for transmission electron microscopy (TEM) analysis to measure interplanar spacings (d) and particle sizes of the powders. Magnetic measurements were performed using a Quantum Design MPMS3 SQUID (superconducting quantum interference device) magnetometer under an applied field of 200 Oe. UV-VIS spectrum of the synthesized powder was obtained through creating a dilute dispersion in water and using a Shimadzu UV-260.

2.4. Computational analysis by density functional theory

In order to investigate the lattice parameters, magnetization density, electronic band structures, density of states, thermodynamic functions and elastic properties of the NdB_6 phases, spin-polarized density functional theory (SP-DFT) was applied in this study. The generalized gradient approximation was utilized as the exchange functional, as parametrized by Perdew, Burke and Ernzerhof (GGA-PBE) [35]. Given that the presence of f-electrons can cause significant challenges due to self-interaction error, we have also computed and benchmarked the lattice parameters and the magnetic properties using hybrid density functional theory, with HSE06 [36] as the exchange functional, which shows consistent results. A planewave cut-off energy of 500 eV was used, with a Gaussian integration scheme and a smearing width of 0.05 eV. A minimum $\mathbf{k}$-point spacing of 0.2 $Å^{-1}$ was applied. During the MCS and its subsequent leaching, there are possibilities for the introduction of intrinsic defects (such as Nd or B vacancies) and/or doping with Mg, H, Cl and O. Therefore, to better understand the changes induced by such defects, their formation energies and magnetic moments have been calculated by using the supercell approach to minimize spurious defect-defect interactions. In order to investigate the d-spacing changes that will be induced by these defects, several supercells are constructed from the primitive structure to $2 \times 2 \times 2$, $3 \times 3 \times 3$ and $4 \times 4 \times 4$ supercells, where dopants are positioned in substitutional (Mg, Cl, O) or interstitial (H) sites. The defect formation energy (ΔH_f^{DFT}) is calculated as proposed by Zhang and Northrup in Eq. (2) [37].

$$\Delta H_f^{DFT} = E_{tot}^{q} - \sum n_i \mu_i + q\left(E_f + E_{VBM}\right) + E_{corr}^{FNV} \quad (2)$$

E_{tot}^{q} is the total energy difference of the defective and pristine supercells. E_f is the equilibrium Fermi energy and E_{VBM} is the valence band maximum, with q being the defect charge. E_{corr}^{FNV} is the FNV correction [38] due to charged defects. Given the overlap of the valence and conduction bands in these structures, charged defects are not considered, because such defects cannot exist under these circumstances [39], hence, $q = 0$ at all times. Therefore, the defect formation energies are directly linked to the chemical potential of their constituent elements (μ_i), as elaborated upon in detail by Freysoldt et al. [40].

The phonon density of states, and consequently the thermodynamic functions (heat capacity, vibrational entropy and enthalpy) were calculated based on the approach proposed by Parlinski, Li and Kawazoe [41]. The elastic constants were calculated by considering strained cells [42,43]. The total energy difference of each strained cell when compared to pristine cell was used, as shown in Eq. (3), based on applied engineering strain e, and changes in ductility are also calculated similar to the methodology applied by Tan et al. [44].

$$E_{tot}^{strained} - E_{tot}^{pristine} = \frac{V_o}{2} \sum_{i=1}^{6} \sum_{j=1}^{6} C_{ij} e_i e_j \quad (3)$$

Here V_o is the initial volume of the cell. The Poisson's ratio, shear (G), bulk (B), longitudinal (M) and Young's (Y) moduli were calculated based on the fundamental principles of elasticity (Voigt-Reuss-Hill model) [45]. The impact of strain on the magnetic moment was analyzed by performing a DOS calculation on the strained cells. For estimating the nano-indentation Vickers hardness values, the empirical model of Chen et al. [46] was applied. Similarly, based on the elastic constants, the thermal expansion coefficient as a function of temperature was calculated through the Grüneisen-Debye approximation [47]. Non-stoichiometry and associated strains are known to cause significant changes in material behavior [48]. Therefore, the elastic properties were also calculated in the case of applying hydrostatic strain on the cell in order to estimate the impact of various strains on the mechanical properties, optical and magnetic properties.

An important property of the hexaboride structures is their work function (∅) [49,50], which has been calculated for the (100) and (111) planes, by considering the changes in the local electron potential across a slab, and the difference in the bulk electron potential when compared to the vacuum level, as shown in Eq. (4) for plane i. The suitability of this approach was recently discussed by Jiang et al. [51].

$$\varnothing_i = V_i^{vac} - E_f \quad (4)$$

For this purpose, seven consecutive cells were considered in a $1 \times 1 \times 7$ supercell, with 10 Å of vacuum between periodic slab images.

In order to estimate the color of synthesized powders under various conditions, we have applied the methodology of Gajdoš et al. [52] for the calculation of the imaginary (ε^i) and real (ε^r) parts of the dielectric function, as a function of photon frequency ω. The real component of the dielectric tensor was then calculated through Kramers-Kroning transformation as shown in Eq. (5). P being the principal value, and η is the complex shift taken as 0.1.

$$\varepsilon^r(\omega) = 1 + \left(\frac{2P}{\pi}\right)\int_0^{\infty} \frac{\varepsilon^i(\omega')\omega'}{\omega'^2 - \omega^2 + i\eta} d\omega' \tag{5}$$

The frequency-dependent absorption coefficient (Λ) is then calculated using Eq. (6) [53], where c is the speed of light in vacuum. The Bouguer-Lambert's law is applied for obtaining the transmission spectra $T(\omega)$ in Eq. (7), with the path length L based on the synthesized particle size.

$$\Lambda_i(\omega) = \frac{\sqrt{2}\omega}{c}\sqrt{\sqrt{\varepsilon^{r2} + \varepsilon^{i2}} - \varepsilon^r} \tag{6}$$

$$T(\omega) = e^{-L\Lambda_T(\omega)} \tag{7}$$

The respective Red Green Blue (RGB) color coordinates were found based on the D_{65} illumination standard, through the conversion of the transmission spectra into XYZ tristimulus values, which were then transformed into RGB values as follows. These calculations were done as in Eq. (8) and Eq. (9).

$$\begin{bmatrix} r \\ g \\ b \end{bmatrix} = 255 \cdot \begin{bmatrix} 3.240 & -1.537 & -0.499 \\ -0.969 & 1.876 & 0.042 \\ 0.056 & -0.204 & 1.057 \end{bmatrix} \begin{bmatrix} X \\ Y \\ Z \end{bmatrix} \tag{8}$$

$$\begin{bmatrix} R \\ G \\ B \end{bmatrix} = \begin{bmatrix} \frac{r}{2} \\ \frac{g}{3} \\ b \end{bmatrix} \tag{9}$$

3. Results and discussions

We have demonstrated the production of superplastic NdB_6 nanostructured powders through the versatile method of MCS via high energy ball milling, which is a simple and room temperature process that also enables the control of product microstructure (phase, shape, size, etc.), and widely used to produce homogeneous materials [30–32,54]. This method can fulfill the requirements for producing superplastic nanostructured NdB_6. The reason for the superplasticity is rooted in the extreme compressive stress that becomes possible through the high energy ball milling. The sequence of the production process highly favors formation of boron vacancies that are crucial for superplasticity. We observe changes in the color and reduced magnetic moment of the NdB_6 due to this production process, the reasons for which are explained through an atomistic perspective in the following sections.

3.1. Properties of pristine NdB_6

The computed lattice parameters, bulk density, formation energy, elastic constants, mechanical properties and magnetic moments of a pristine NdB_6 lattice, as calculated by DFT, are listed in Table 1. The calculated mechanical properties show that NdB_6 is a hard and brittle material, with a purple color appearance, as known experimentally. A schematic of the atomic arrangements in NdB_6 lattice, and its electronic density of states (DOS) are shown in Figs. 2a and 2b, respectively. The DOS illustrates a significant asymmetry in the contribution of the spin-up versus spin-down f-electrons, which is the primary reason for the high magnetic moment of this boride phase. There are also allowed unoccupied levels right after valence band maximum (Energy = 0 is the Fermi level), making NdB_6 electrically conductive as well. The calculated magnetic moment is also in agreement with prior experimental studies [7]. The heat capacity, thermal expansion coefficient and vibrational entropy of the NdB_6 are given in Figs. 2c and 2d, which are in close agreement with prior experimental thermodynamic studies [19].

3.2. Computationally aided experimental design

In order to model and optimize the production process, the CALPHAD method was used for modelling reaction products between the reactants used, namely Mg, B_2O_3 and Nd_2O_3. The adiabatic temperature of the system for Eq. (1) was calculated

Table 1 – Properties of the NdB_6 phase as predicted by DFT.

Table 1. Properties of the NdB_6 phases as predicted by DFT.

Property	Pristine NdB_6
Lattice parameters (Å)	$a = 4.134$
Space group	Pm-3m
Bulk density (g/cm^3)	4.914
Zero point energy, ZPE (eV)	0.438
Work function, Ø at 0 K (eV)	3.37 (100) 3.33 (111)
Magnetic moment (μ_β/f.u.)	3.195
Elastic constants (GPa)	$C_{11} = 468.33 \pm 3.42$ $C_{12} = 27.12 \pm 3.42$ $C_{44} = 65.78 \pm 4.83$
Bulk modulus (GPa)	174.19
Shear modulus (GPa)	109.58
Young's modulus (GPa)	270.70
Poisson's ratio	0.240
Pugh's ratio	1.590
Vickers hardness (GPa)	15.15
Thermal expansion (10^{-6}/K)	8.662 (at 298 K) 11.124 (at 1000 K)
Grüneisen parameter	1.453
Debye temperature (K)	721.30
Color	Purple

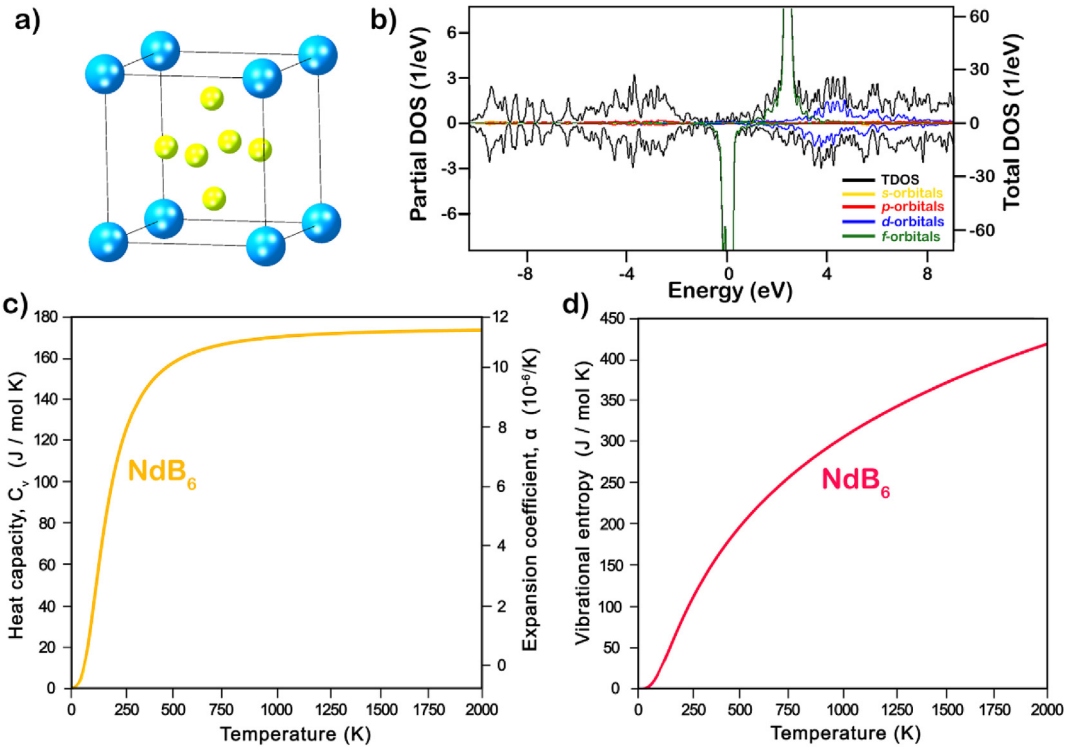

Fig. 2 – Schematic of the atomic arrangements of pristine NdB_6 (a). The blue atoms show Nd, and lime color atoms represent B, as well as the DOS (b) and thermodynamic properties of NdB_6 (c,d).

as 2834 °C with the increasing B_2O_3 content, which shows the extremely exothermic nature of this reaction. The ΔH and ΔG values were calculated to be −3904.9 kJ/mol and −3751.3 kJ/mol at 25 °C, respectively. Fig. 3a elucidates the equilibrium reaction products as a function of temperature. Given the non-adiabatic nature of the experimental set-up, which is known to reach a temperature of approximately 600 °C, varying B_2O_3 contents were also considered (Fig. 3b). It is noteworthy that higher synthesis temperatures are found to cause gasification of precursors such as B_2O_3 and Mg, which should be avoided. Fig. 3b demonstrates the simulated reaction product stoichiometries (Eq. (1), $A = 6$ mol) at varying temperatures under 1 atm atmospheric pressure. It was found that between 25 °C and 400 °C, two boride phases form, mainly NdB_4 together with $Mg(B_6)_2$. Also, the reduction product MgO forms, with minor quantities of $Mg_3B_2O_6$ as well as retained

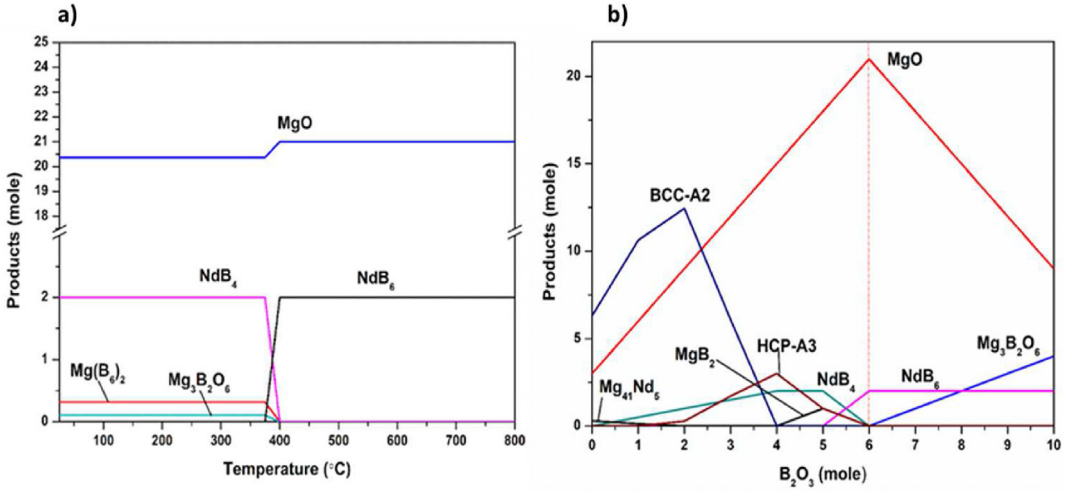

Fig. 3 – Thermochemical simulation of the reaction products for the stoichiometric powder blend (a), the effect of varying B_2O_3 content at a fixed temperature of 600 °C (b), dashed line corresponds to the stoichiometric powder blend.

Table 2 – DFT calculated defect formation energies along with their equilibrium concentrations and magnetic moments in NdB_6 for a 2 × 2 × 2 supercell.

Defect	ΔH_f (eV)	ΔH_f* (eV)	Equilibrium conc. ($N_d/N_s \times 10^6$)	Magnetism (μ_B/f.u.)
V_{Nd}	$9.88 + \mu_{Nd}$	38.94	0	2.95
V_B	$7.72 + \mu_B$	− 5.70	*Phase decomposition*	1.67
Mg_{Nd}	$9.81 + \mu_{Nd} - \mu_{Mg}$	45.94	0	3.10
Mg_B	$16.51 + \mu_B - \mu_{Mg}$	10.18	10^{-53}	1.79
Mg_i	$2.52 - \mu_{Mg}$	9.61	10^{-50}	3.53
Cl_B	$10.89 - \mu_{Cl} + \mu_B$	− 3.60	*Phase decomposition*	0.60
O_B	$2.91 - \mu_O + \mu_B$	− 5.70	*Phase decomposition*	3.38
H_i	$0.063 - \mu_H$	4.77	10^{-22}	2.54
$V_{Nd} + H_i$	$11.34 - \mu_H + \mu_{Nd}$	29.06	0	« 1
$V_B + H_i$	$5.50 - \mu_H + \mu_B$	− 3.22	*Phase decomposition*	« 1

excess B_2O_3. This suggests that the complete reduction of B_2O_3 phase may not be achieved at low temperature range. Above this critical temperature (400 °C), the aimed NdB_6 phase is obtained as the sole product of the reaction, if the B_2O_3 content is well controlled. The CALPHAD model shows the thermodynamic possibility of achieving NdB_6 under the experimental set-up used, which can be purified through leaching in HCl solution for dissolving the MgO by-product.

The use of HCl acid during leaching and the significant formation of Mg-related phases during the production process warrant a study on the changes in the lattice by doping H, Cl, Mg or O. The defect formation energies for some of the possibilities that seem likely are listed in Table 2. The calculations illustrate that it is rather unlikely for Mg atoms to occupy Nd sites, given the reference chemical potentials considered for the experimental set-up used. Placement of Mg as anti-site defect (taking over B sites) is more likely, although the defect formation energy is extremely high, and makes such defects rather inconsequential, given the Arrhenius relationship for the equilibrium defect concentrations in Eq. (10). A defect can occupy within the crystal, considering the N_d and N_s terms are the number of defects per unit volume and the total number of sites, respectively.

$$\frac{N_d}{N_s} = e^{\left(\frac{-\Delta H}{k_B T}\right)} \tag{10}$$

The calculations also show that the defect formation energies of Cl and O that occupy a B site are negative, which translates to the extremely high likelihood of such defects, and the eventual phase decomposition of NdB_6, if the kinetic barrier for the formation of such defects is low enough. The phase decomposition is apparent from Eq. (3) as well, because if $\Delta H_f < 0$, then $N_d > N_s$, which is unphysical. The defect concentrations due to these dopants depends on the chemical potential of the elements Eq. (2), and therefore the defect formation energies are tabulated as a function of the chemical potentials in Table 2, and also given for conditions where chemical potentials are referenced to their compatible phases that are shown in Fig. 4. In other words, the chemical potentials of Mg, B, H and Cl are referenced to $Mg_3B_2O_6$, MgO, H_2O, HCl and O_2 gas, as demonstrated below in Eq. (11) to Eq. (16), which is simply based on our experimental set-up.

$$\mu_B = \frac{1}{2}\left(\mu_{Mg_3B_2O_6} - 3\mu_{Mg} - 6\mu_O\right) \tag{11}$$

$$\mu_{Mg} = \mu_{MgO} - \mu_O \tag{12}$$

$$\mu_{Nd} = \mu_{NdB_6} - 6\mu_B \tag{13}$$

$$\mu_H = \frac{1}{2}\left(\mu_{H_2O} - \mu_O\right) \tag{14}$$

$$\mu_{Cl} = \mu_{HCl} - \mu_H \tag{15}$$

$$\mu_O = \frac{1}{2}\mu_{O_2} \tag{16}$$

These references are based on the abundance of O_2 gas, and HCl during MCS and leaching, as well as the compatible phases that have been calculated by FactSage. It should be noted that ΔH_f* values of Table 2 are formation energies that are based on chemical potentials given in Eq. (11) to Eq. (16). However, the ΔH_f column that keeps the chemical potentials as variables can be used for any other experimental condition. The calculations demonstrate that the most likely simple point defects that may occur are V_B (B vacancy), Cl_B (Cl positioned in B site), O_B (O positioned in B site), and $V_B + H_i$ (B vacancy filled with H interstitial). A schematic representation of the defect structures is shown in Fig. 4. As explained above, to achieve our aim for synthesizing a ductile boride, the formation of B vacancy is crucial, and the production process designed here allows such defects to form, which would be otherwise challenging when considering the stability of borides and their strong covalently bonded structures.

The theoretical predictions of Pan et al. [29] show an increasing Pugh's ratio (ratio of bulk to shear modulus) as boron vacancy concentration increases in ReB_2. This was attributed to reduced lattice parameters that lead to weak hybridization between metal cation and boron. However, they have also predicted difficulties in creating such defects. Therefore, by using a high energy ball mill during MCS, instead of a low speed mill such as planetary ball mill, it is possible to forcefully reduce the lattice parameters by compressively straining the unit cells. Hence, we chose high energy ball mill under the framework of MCS for this study, which can facilitate the desired compressive strains through inducing B-vacancies.

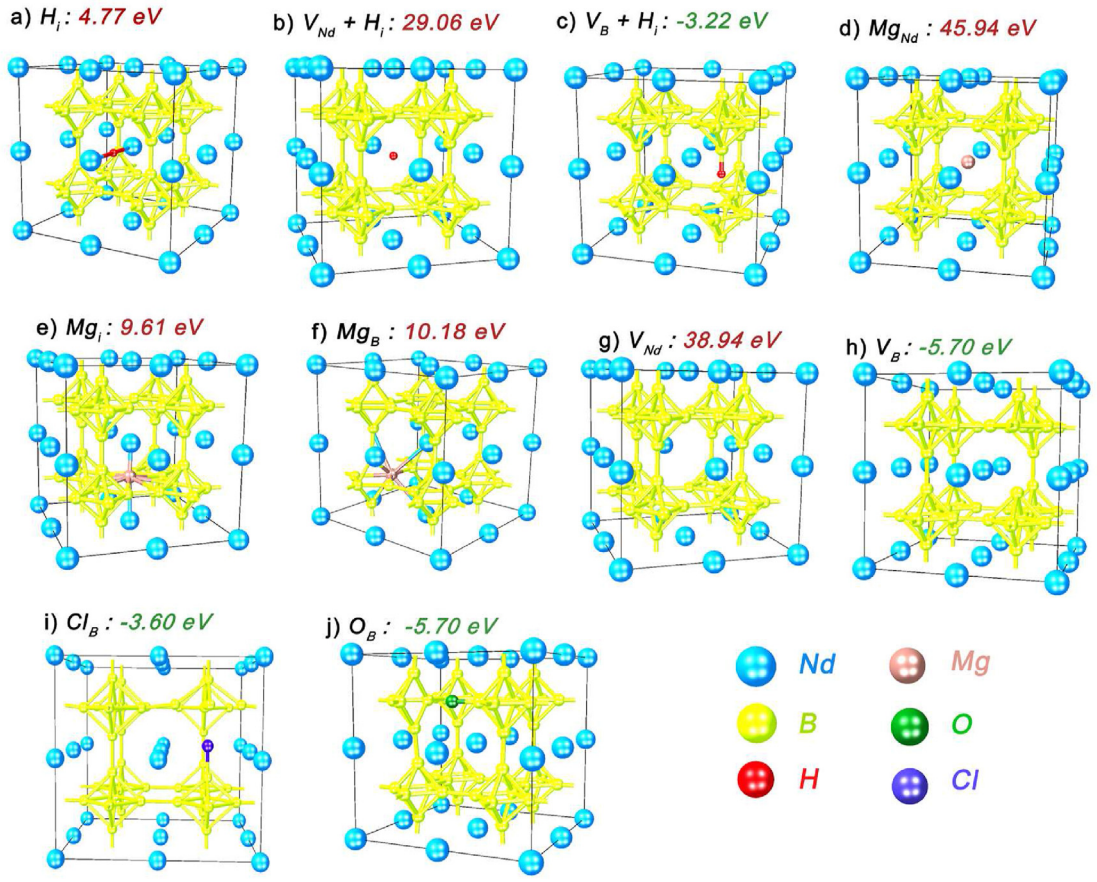

Fig. 4 – Defect structures of NdB_6 considered based on the possible dopants due to the MCS process used. The defects with formation energies colored in green are highly probable.

The MCS method is known to induce residual lattice strains and a plethora of studies on this topic have elucidated the inevitability of strain induced structures through either mechanical or defect induced means [55]. MCS provides an excellent flexibility on the chemical potential equilibria, simply based on the precursors and environment that are used during synthesis (see Eq. (11) to Eq. (16)). Given the prevalence of B-vacancy in the structure as per our DFT calculations (Table 2), and the eventual appearance of compressive strains due to B-vacancies that were also validated experimentally (shown in the following sections through TEM investigations), we estimated the changes in the elastic constants due to various local strains through DFT. The prevalence of strain dependent materials properties is a widely studied phenomenon, and it is known that strains at the atomic level can significantly alter mechanical, optoelectronic and even catalytic properties [48,56]. It is noteworthy that chemically induced strains (through defects) are not necessarily an intrinsic outcome of the MCS production method [30,54], but rather an effect of the chemical potential equilibria that emerges during synthesis. Therefore, this study demonstrates that it is possible to use the MCS along with certain precursors and environmental conditions that yield chemical potentials of interest for facilitating defects of interest. Thus, inducing strains that are otherwise not possible, make MCS a viable method for strain engineering. We conducted the DFT calculations based on relaxing cell parameters under hydrostatic stresses. It is found that NdB_6 shows superplasticity if the cell is compressively strained such that the lattice is under compressive stresses beyond 15 GPa (as shown in Fig. 5a). The main reason for this phenomenon is the change in C_{44} as a function of applied stress, which approaches zero under extreme compression. This is a sign of superplasticity as proposed by Saito et al. [57] and Souvatzis et al. [58]. In fact, the main reason is diminishing critical shear stress, which approaches zero as C_{44} approaches zero. Therefore, through the application of MCS using high energy ball mill, we have theoretically predicted that it is possible to synthesize superplastic NdB_6, if the lattice is sufficiently compressed, either by external stress or chemical doping or defects. This is also verified by considering the variations in the Pugh's ratio [59] (Fig. 5b), which shows compressive strains cause a transition from brittle to ductile behavior.

3.3. *Phase analysis of synthesized powders*

The XRD patterns of the as-blended Nd_2O_3–B_2O_3–Mg powders, and those MCS'd for different durations up to 4 h are shown in Fig. 6a. In the XRD pattern of the as-blended (non-milled) powders, Nd_2O_3 (ICDD Card No: 00-043-1023, Bravais

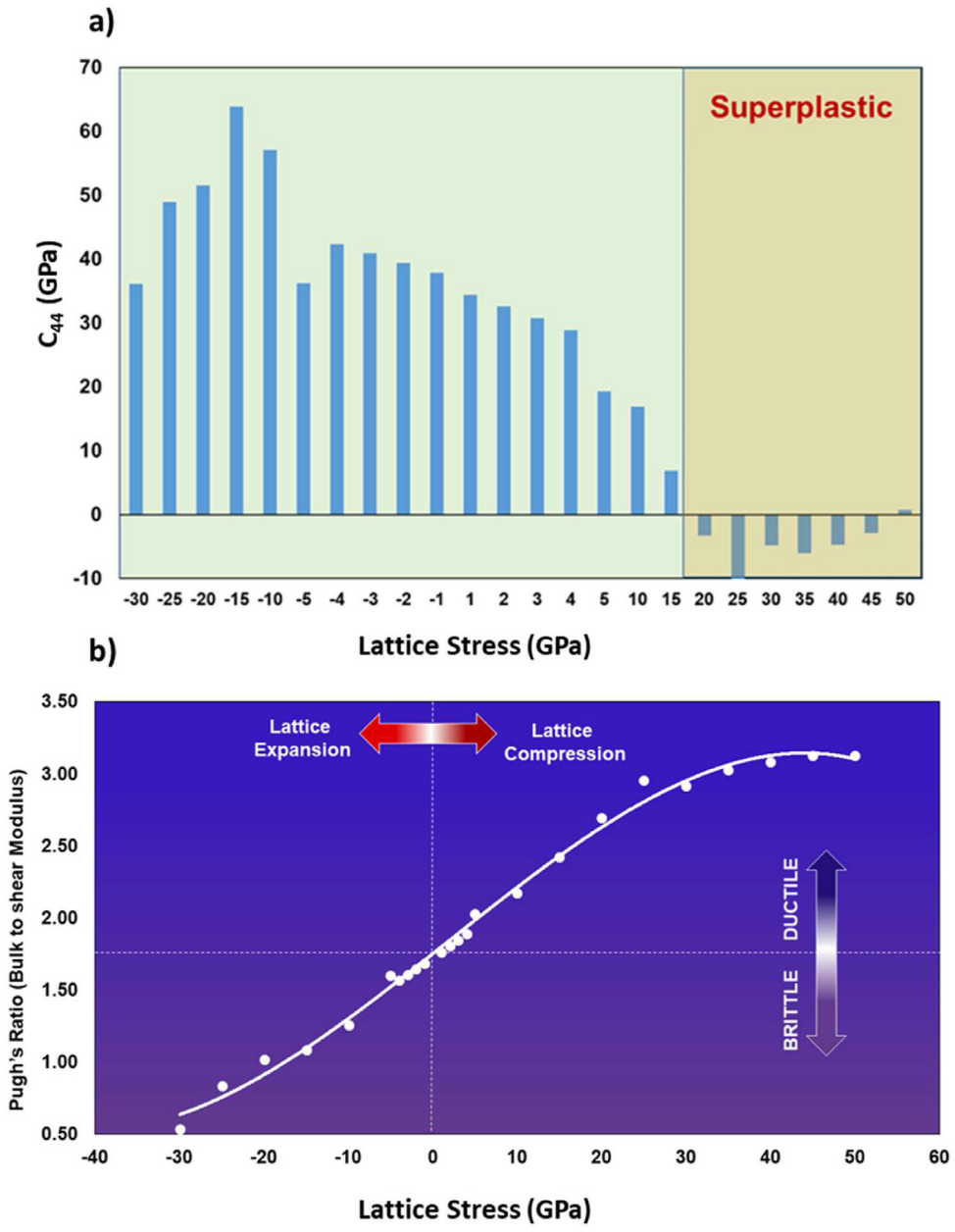

Fig. 5 – Variations in C_{44} as a function of hydrostatic stress (a). The negative stresses are tensile, and the positive values are compressive. Superplasticity is inevitable as C_{44} approaches zero, which is further supported by the changes in the Pugh's ratio (bulk to shear modulus ratio), which demonstrates a transition from brittle to ductile behavior under compressive strains as well (b).

lattice: primitive hexagonal, $a = 0.382$ nm and $c = 0.599$ nm), Mg (ICDD Card No: 00-004-0770, Bravais lattice: primitive hexagonal, $a = 0.321$ nm and $c = 0.521$ nm) and $Nd(OH)_3$ (ICDD Card No: 01-083-2035, Bravais lattice: primitive hexagonal, $a = 0.329$ nm and $c = 0.521$ nm) phases were detected, as expected. The characteristic peaks of B_2O_3 were not observed in the XRD pattern of the as-blended powders because of its amorphous nature. The intensities of the Nd_2O_3 and Mg phases decreased with increasing milling time. This indicates a reduction in the average crystallite sizes of the Nd_2O_3 and Mg powders, and hence an increase in their reactivity for the forthcoming reduction reaction. Also, $Nd(OH)_3$ phase is no longer observed as the milling time increases. As seen from Fig. 6a, the powders milled for 1 h contain Nd_2O_3, MgO (ICDD Card No: 01-079-0612, Bravais lattice: face centered cubic, $a = 0.422$ nm), NdB_6 (ICDD Card No: 03-065-1828, Bravais lattice: primitive cubic, $a = 0.413$ nm) and NdB_4 (ICDD Card No: 00-024-1458, Bravais lattice: tetragonal, $a = 0.722$ nm and $c = 0.410$ nm) phases. Besides, the intensity of MgO phase is higher for the 1 h milled powders compared to those of other

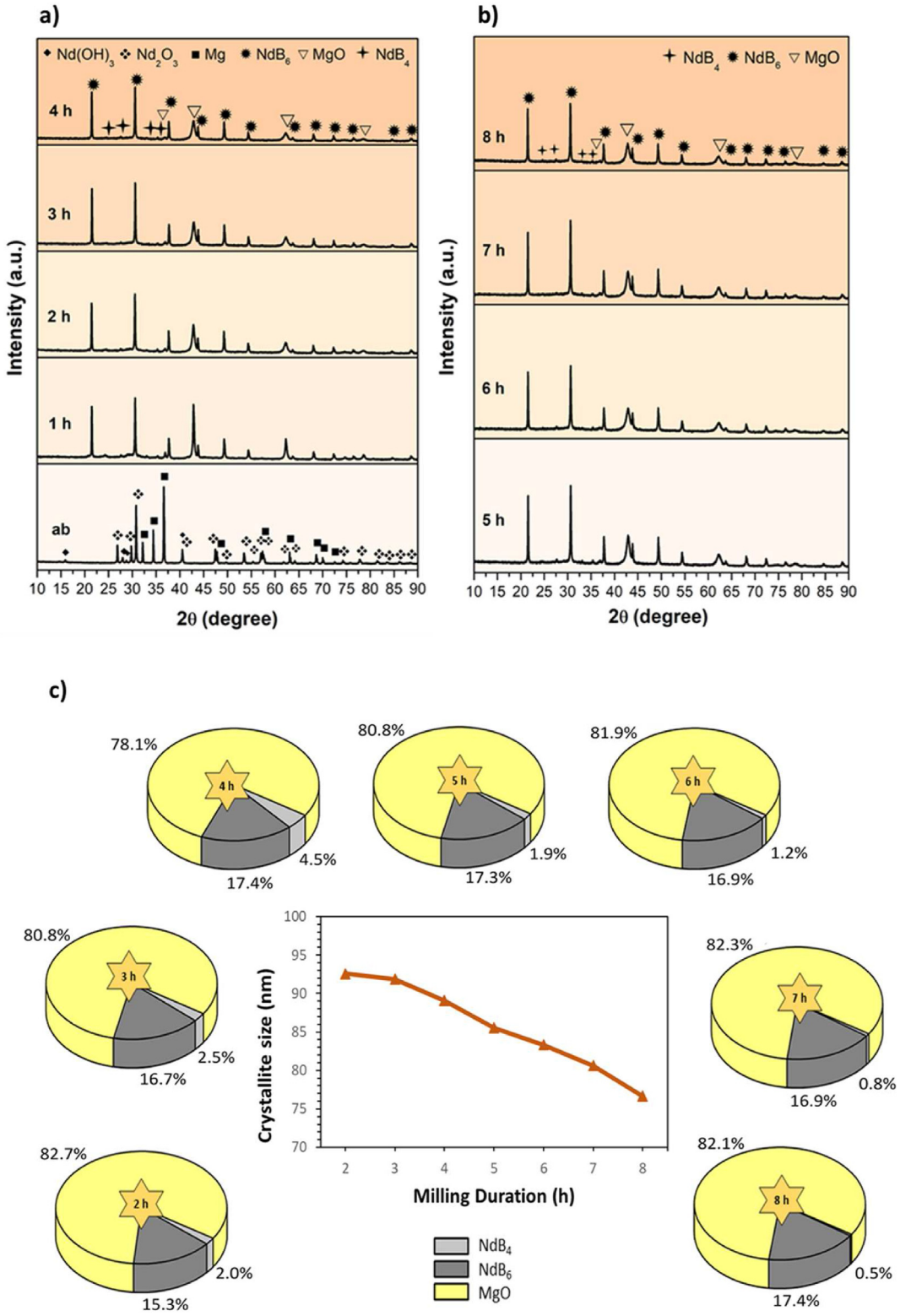

Fig. 6 – XRD patterns of the (a) as-blended Nd_2O_3–B_2O_3–Mg powders and those mechanochemically synthesized for 1 h, 2 h, 3 h and 4 h and (b) 5 h, 6 h, 7 h and 8 h, (c) Average crystallite sizes of NdB_6 phase in the mechanochemically synthesized powders versus milling duration plots, and corresponding Rietveld analyses showing the NdB_6, NdB_4 and MgO phase weight percentages.

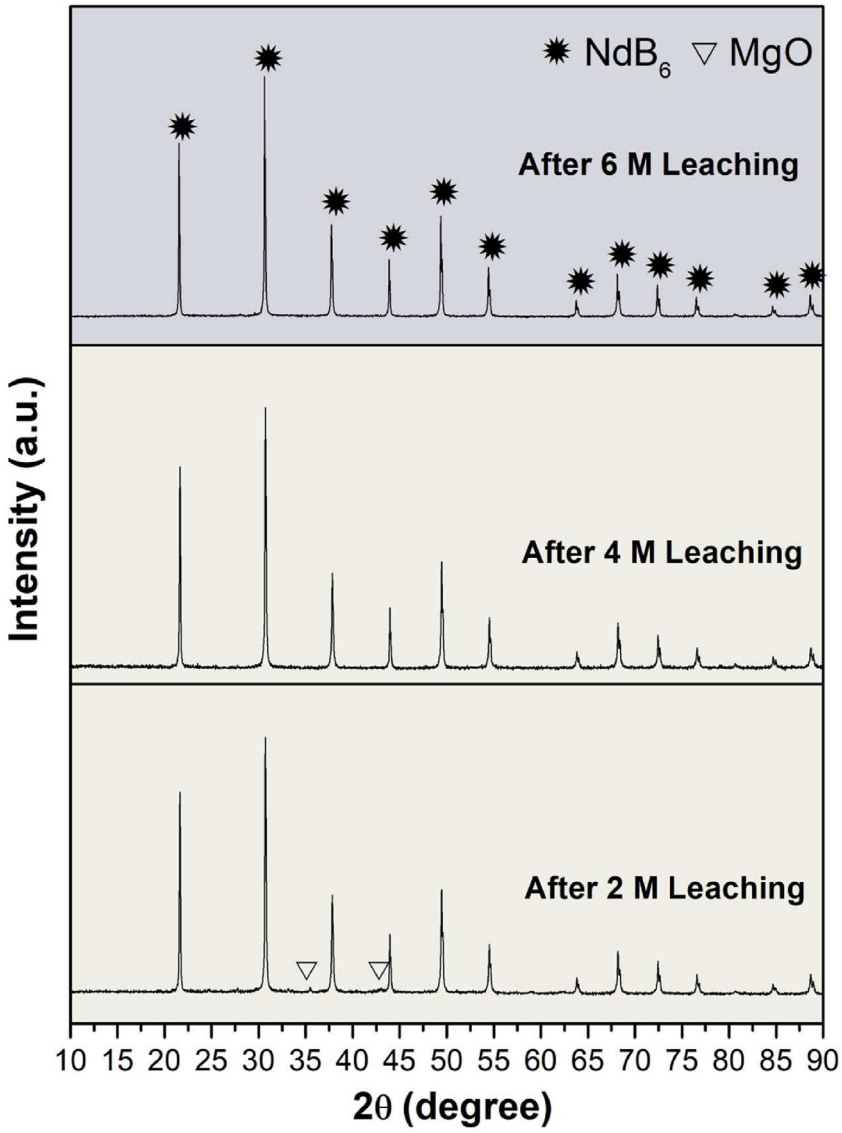

Fig. 7 – XRD patterns of the NdB_6 powders after 2 M, 4 M and 6 M HCl leaching. This powder is originated from Nd_2O_3–B_2O_3–Mg blends mechanochemically synthesized for 5 h.

milling times. After 1 h, the intensity of MgO phase became more stable and comparable with each other. Therefore, 1 h milling duration can be considered as the initial point for the formation of the boride phases. At the end of 3 h milling, the only detected phases were mostly NdB_6 and MgO along with minor amounts of NdB_4 (Fig. 6a). XRD pattern of the 5 and 8 h milled powders are illustrated in Fig. 6b, showing that extended milling duration did not change the nature of the resulting products, as NdB_6 and MgO phases are still present with NdB_4 phase, and no new phases have formed. Besides, the peak intensities of the NdB_6 and MgO phases gradually decreased from 5 to 8 h milling as seen from Fig. 6b, that may be attributed to the crystallite size reduction due to the high and repeated impact energy acquired during milling. Although the NdB_6 phase formation starting from different raw materials was previously reported in the literature [13,23,24,27], the occurrence of NdB_4 with NdB_6 is being reported for the first time. The reason for the observed phase transformations is well-explained through the thermochemical CALPHAD calculation through FactSage. The average crystallite sizes and phase analyses of the powders milled for different durations are shown in Fig. 6c. The most intense five peaks (diffracted from (100), (110), (111), (200) and (210) planes) were selected for the TOPAS measurements. On the basis of the related XRD patterns, the average crystallite sizes of the NdB_6 phase in the powders milled for 2–8 h were calculated as 92.6, 91.86, 89.08, 85.52, 83.32, 80.62 and 76.68 nm, respectively. Also, after 5 h of milling time, the amounts of NdB_6, NdB_4 and MgO phases no longer show significant changes based on the Rietveld analyses. Therefore, 5 h was chosen as the optimum milling time.

In order to dissolve the unwanted reaction product (MgO), leaching was done. Different molarities of HCl acid were also tried for leaching. XRD results are given in Fig. 7. MgO phase

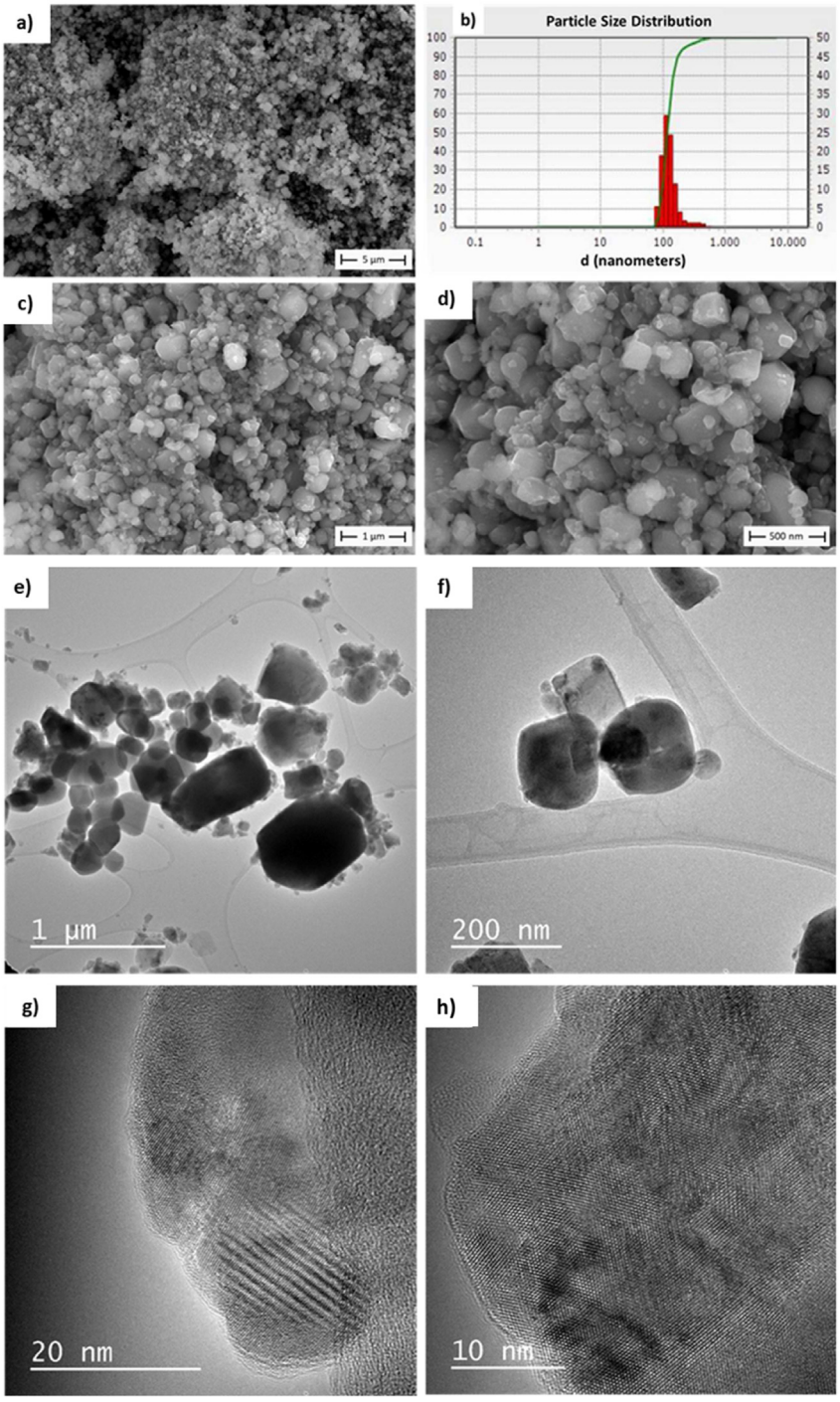

Fig. 8 – SEM image of the NdB_6 powders under 13,000×magnifications (a) and the particle size distribution (b) followed by SEM images under magnifications of 50,000×(c), 100,000×(d) and TEM images for NdB_6 leached with 6 M HCl acid (e–h).

was observed in the 2 M leached powders. However, impurities were no longer observed in the 4 M leached powders. Therefore, 4 M HCl acid solution was chosen for further leaching treatments. As clearly seen in the XRD pattern of the NdB_6 powders that are MCS'd for 5 h and leached with 4 M HCl, the acid concentration is sufficient to remove the MgO phase completely from the powders. On the other hand, no impurity phases were observed in the XRD pattern within the detection limit of the used diffractometer (<2 wt %). Moreover, based on the XRD pattern, the average crystallite size of the 4 M leached powders was determined as 117.3 nm.

Table 3 – The variations in d-spacings due to the defects that are probable based on DFT and measured EDS values.

Structures	Planes		
	d (100) (Å)	*d* (110) (Å)	*d* (111) (Å)
Pristine NdB_6	4.143	2.929	2.392
0.62% B-Vacancy	4.146	2.931	2.393
2.08% B-Vacancy	4.135	2.924	2.384
5.50% B-Vacancy	4.085	2.917	2.379
8.33% B-Vacancy	3.632	2.746	2.296
0.22 at % Cl	4.137	2.926	2.393
0.53 at % O	4.141	2.928	2.398

Upon comparing the results of this study with the published literature, it is seen that NdB_6 phases are produced only through demanding procedures that require high temperature (1500 °C for 4 h holding time) [13], or application of pressure (20 MPa) through combustion synthesis [23]. Similarly, boron-rich RE boride, NdB_6 was synthesized at 1600 °C and 4.0 GPa pressure at a duration of 1.5 min [27]. These methods require considerable time and energy to reach the synthesis temperature and to complete the reactions, hence from the perspective of green and eco-friendly technologies, the production of NdB_6 is significantly more advantageous through the method proposed here, which may be further extended into other rare earth hexaborides through future research. Moreover, any process that requires high temperatures will anneal the strains, and thus a superplastic NdB_6 (as shown in Fig. 5) cannot become possible.

3.4. *SEM, TEM and lattice compression observations*

Fig. 8 shows SEM images with different magnifications (13,000, 50,000 and 100,000 ×). Particle shape was seen in mixed

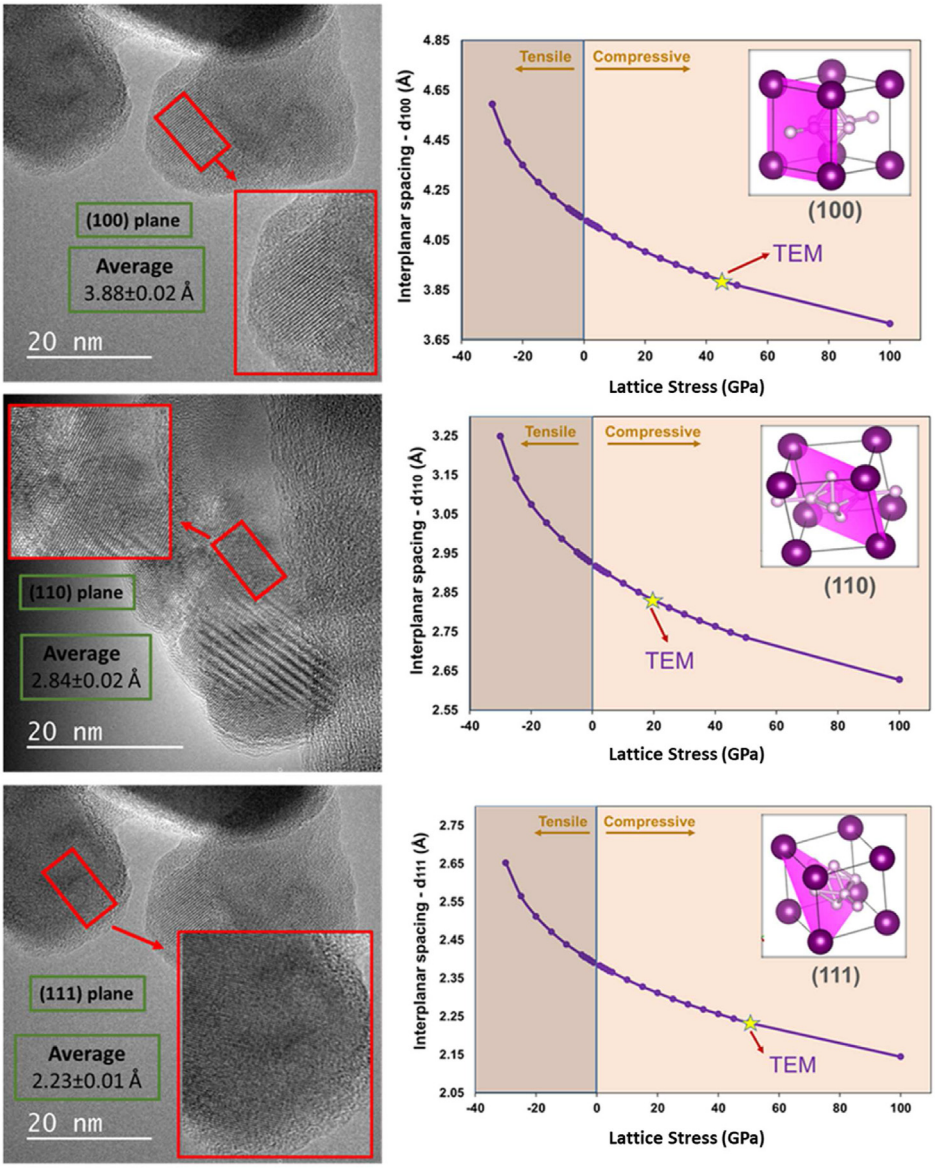

Fig. 9 – TEM images for NdB_6 leached with 6 M HCl acid, as correlated with DFT calculated interplanar spacings for (100), (110) and (111) planes under various lattice stresses.

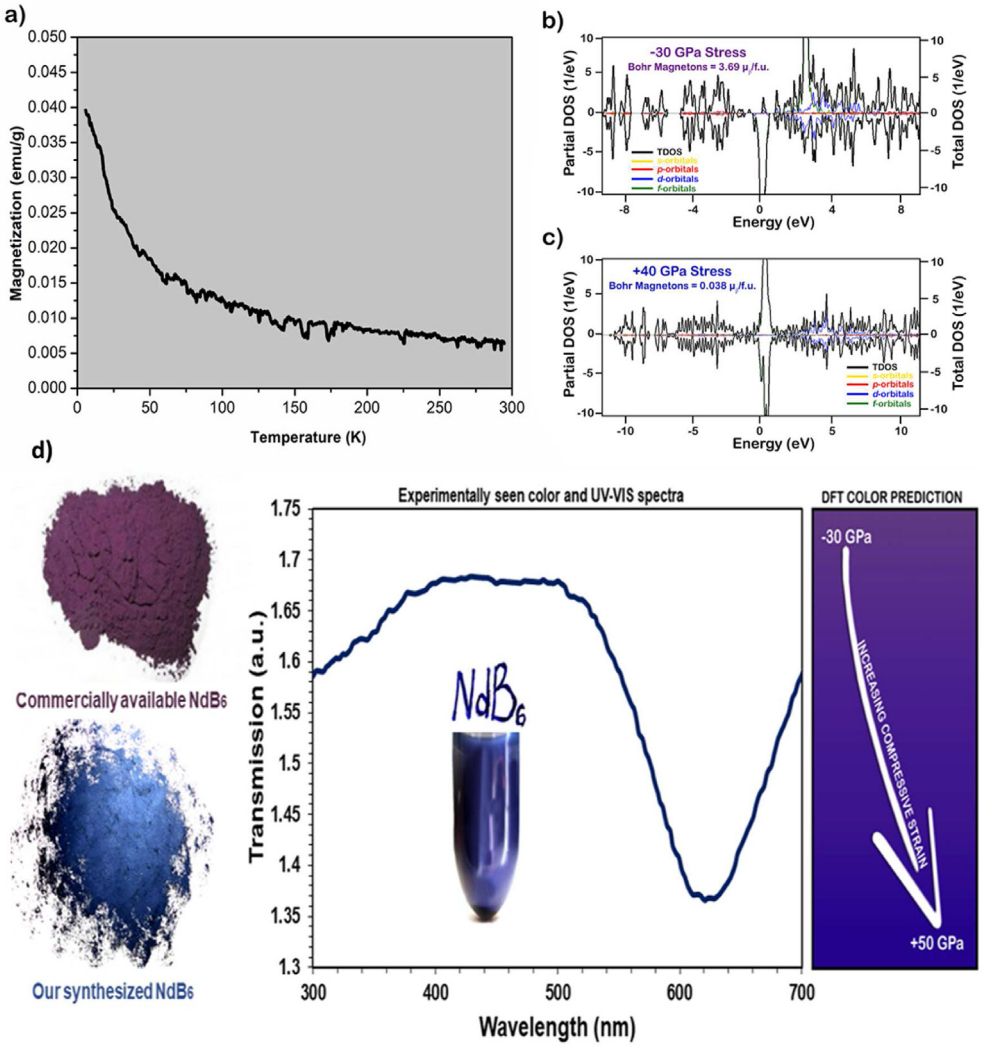

Fig. 10 – Experimental magnetic moment analysis for NdB_6 leached with 6 M HCl acid (a), explained through changes in DOS due to stress as calculated by DFT (b,c), experimentally obtained UV-VIS spectra, with an inset photograph of the synthesized powders, and DFT computed changes in color as a function of stress are shown (d).

morphology according to the SEM images. The general EDS analysis taken from the area in Fig. 8c reveals the amounts of Nd, B, O, Mg and Cl elements as 24.95, 72.39, 2.4, 0.18 and 0.08 at %, respectively. This shows significant B vacancy as the pristine structure must contain ~86 at % B. In addition, the PSA graph as given in Fig. 8b illustrates that the average particle size of the NdB_6 was about 118.9 nm which is in the similar range observed in the SEM image in Fig. 8c. Lognormal distribution type was observed for this graph. Higher magnification of SEM image (Fig. 8d) for NdB_6 shows particle size between 80 and 120 nm. Also, the tap density of NdB_6 powders was measured as 4.03 ± 0.01 g/cm^3. This rather large particle size (Fig. 8d) and quite dense interior (4.03/4.95 = 81.4%) indicate the malleability of the NdB_6 produced, which must undergo cold welding at room-temperature. TEM images are given in Fig. 8e–h, with the average particle sizes found to be smaller than 200 nm. Also, particle shape is once again seen to be in various mixed morphologies. Considering the EDS and defect formation energies, we have also analyzed the changes in *d*-spacing that should be expected based on a full geometry relaxation through DFT, as shown in Table 3. It is clear that boron vacancy causes significant contraction in *d*-spacing.

TEM offers the opportunity to measure interplanar spacings experimentally. Multiple samplings were made from different areas. For each area, a minimum of five measurements were done, and the results are given in Fig. 9. For (100), (110) and (111) planes, the interplanar spacings given in crystallographic databases, and PDF-cards are 4.128, 2.919 and 2.383 Å, respectively [60]. However, these values do not match with our experimental measurements, and the synthesized nanopowders show significantly smaller interplanar spacing, demonstrating the compressive strain, as anticipated. The changes in interplanar spacing as a function of stress were calculated using DFT, and the results are shown in Fig. 9. Bringing together the TEM interplanar spacing data and DFT prediction of spacing changes due to stress, shows that the

Table 4 – Changes in lattice parameter, elastic properties, magnetic moment and color due to applied hydrostatic stress on pristine NdB_6 lattice, as calculated by DFT.

Table 4. Changes in lattice parameters, elastic properties, magnetic moment and color due to applied hydrostatic stress on pristine NdB_6 lattice, as calculated by DFT.

Stress (GPa)	a (Å)	C_{11} (GPa)	C_{12} (GPa)	C_{44} (GPa)	Bulk (GPa)	Young's (GPa)	Shear (GPa)	Poisson's ratio	Pugh's ratio	Hardness (GPa)	Magnetic Moment (μ_B/f.u.)	Color coordinates (R, G, B)
-30	4.595	150.6	-28.9	36.1	30.9	106.6	57.6	-0.075	0.537	41.3	3.6901	98, 58, 142
-25	4.443	237.3	-17.9	48.9	67.1	172.3	80.4	0.0721	0.835	29.2	3.4940	80, 52, 145
-20	4.35	293.9	-7.7	51.5	92.9	206.1	91.2	0.131	1.019	24.4	3.4373	107, 59, 165
-15	4.28	338.9	2.3	63.9	114.5	242.5	105.7	0.147	1.083	24.8	3.4235	104, 57, 167
-10	4.226	381.5	12.7	57.1	135.6	256.1	107.9	0.185	1.256	20.7	3.4242	102, 57, 165
-5	4.177	405.1	29.9	36.2	154.9	240.3	96.8	0.242	1.602	13.7	3.4429	82, 54, 169
-4	4.168	412.1	32.3	42.3	158.9	250.7	101.3	0.237	1.568	14.6	3.4383	84, 55, 170
-3	4.159	418.7	34.7	40.9	162.7	251.8	101.4	0.242	1.605	14.1	3.4310	87, 56, 171
-2	4.151	425.3	37.1	39.4	166.4	252.6	101.3	0.247	1.643	13.7	3.4241	88, 57, 172
-1	4.143	431.8	39.3	37.8	170.2	253.3	101.2	0.252	1.682	13.2	3.4216	89, 57, 172
1	4.127	444.5	44.1	34.4	177.5	254.1	100.7	0.261	1.763	12.3	3.4182	89, 57, 173
2	4.119	450.7	46.4	32.6	181.2	254.3	100.4	0.266	1.803	11.8	3.4171	89, 58, 173
3	4.112	456.8	48.8	30.8	184.8	254.4	100.1	0.271	1.846	11.5	3.4170	90, 57, 175
4	4.105	462.9	51.1	28.9	188.4	254.3	99.7	0.275	1.889	11.1	3.4132	88, 57, 173
5	4.098	468.7	53.4	19.3	191.8	243.9	94.7	0.288	2.027	9.5	3.4145	89, 57, 175
10	4.064	497.9	65.4	16.9	209.6	251.3	96.6	0.301	2.169	8.7	0.1083	36, 47, 153
15	4.032	526.2	77.8	6.9	227.3	247.6	93.9	0.318	2.421	7.1	0.1042	32, 44, 150
20	4.003	553.1	89.9	-3.25	244.3	242.1	90.7	0.335	2.694	5.8	0.0564	32, 41, 148
25	3.977	579.2	102.1	-11.5	261.1	238.5	88.5	0.348	2.951	4.8	0.0759	33, 38, 145
30	3.953	604.8	114.4	-4.8	277.8	256.4	95.2	0.346	2.917	5.2	0.0686	35, 35, 143
35	3.931	628.1	125.4	-6.1	292.9	261.8	96.9	0.351	3.024	4.9	0.0515	36, 33, 140
40	3.909	653.7	137.5	-4.7	309.6	271.9	100.4	0.354	3.082	4.9	0.0383	34, 32, 135
45	3.888	678.6	148.9	-2.9	325.5	282.4	104.2	0.355	3.124	5.1	0.0277	37, 29, 132
50	3.869	703.8	160.1	0.7	341.4	295.9	109.1	0.356	3.128	5.2	0.0135	37, 28, 128

synthesized material is under compressive stresses of more than 20 GPa, which coincides with the threshold for superplasticity.

3.5. *Magnetic and elastic properties, and color variations due to lattice strains*

The magnetic moment of NdB_6 was experimentally measured by Stankiewicz et al. [7] as 3.15 μ_B/f.u., which is in good agreement with our DFT computed value of 3.195 μ_B/f.u. For the pristine cell, further validating the computational methodology used in this study. However, the experimentally measured magnetic moment of the NdB_6 synthesized in this study is lower by orders of magnitude as seen in Fig. 10a. This radical decrease is explained when considering the changes in the DOS due to strain. Although boron vacancies and hydrogen interstitials can reduce the magnetic moment as well (Table 2), the fundamental cause is attributed to the changes induced in lattice parameters due to the defects. For a lattice under tensile strain (Fig. 10b), a rise in the magnetic moment is inevitable, however, for compressive strain, a steep fall in magnetic moment is seen. The spin channels become highly symmetric as compressive strain increases, causing a fall in the magnetic moment. Given that the main cause of this fall in the magnetic moment is compressive strain, it is possible to recover the magnetic property through annealing treatments, preferably at high temperatures. Color is another interesting change that is seen in the synthesized powders. Pristine NdB_6 is known for its purple color, which was also successfully predicted by the computational methodology used in our study. However, as the lattice goes through compressive strains, the red component of the RGB color coordinates is reduced, and the color shifts to a vivid blue, as predicted by the DFT calculations shown in Table 4. This is in direct agreement with our experimental observations, as the color of the synthesized powder is vivid blue as well.

4. Conclusions

In the present study, superplastic nanostructured NdB_6 ceramic powders were successfully prepared through a simple two-step process that includes mechanochemical synthesis via high energy ball mill, followed by purification through HCl leaching. The results of this study can be summarized as follows.

- A novel and simple process for synthesizing superplastic nanostructured NdB_6 ceramic powders was achieved by

mechanochemical reaction of powder blends containing stoichiometric amounts of Nd_2O_3, B_2O_3 and Mg powders.
- During the mechanochemical processing of Nd_2O_3, B_2O_3 and Mg starting powders, the formation of the NdB_6 phase started only after 1 h of milling. Extending the milling duration to 5 h resulted in the major NdB_6 and MgO phases in addition to the minor NdB_4 phase, as predicted by the CALPHAD calculations.
- Powders milled for 5 h were successfully purified by leaching in 6 M HCl resulting in the formation of high-purity NdB_6 powders with mixed rounded-shape morphology (average size of 118.9 nm) free from undesired MgO.
- According to the DFT calculations, formation of boron vacancy is highly favorable under the applied mechanochemical synthesis conditions, which causes compressive strains in the NdB_6 lattice.
- It is found that the NdB_6 becomes superplastic as C_{44} approaches zero under the chemically induced compressive lattice stresses of more than 15 GPa, followed by a significant reduction in hardness and increase in the Young's modulus.
- The magnetic moment of the synthesized powder is seen to be orders of magnitude lower than that of the pristine NdB_6. This annihilation of the magnetic moment is explained through the density of states (DOS) calculations on the compressively strained NdB_6 lattice, which demonstrate a similar reduction trend in the magnetic moments.
- The color of pristine NdB_6 is known to be purple, however, the color of the synthesized powders is blue. The DFT calculations on the dielectric function show a transition from purple to blue under compressive lattice stresses of more than 10 GPa, verifying the experimental observations.

Author contributions

B.B. performed formal analysis, investigations, writing-original draft preparation. M.M. performed DFT investigations, conceptualization, writing-original draft preparation. F.K. investigated FactSage and performed formal analysis. E.T. performed analysis. M.H. performed magnetic analysis. M.L.Ö. performed reviewing and editing. J.L. performed conceptualization, reviewing and editing. D.A. supervised, performed project administration, conceptualization, writing-original draft preparation.

Notes

The authors declare no competing financial interest.

Declaration of competing interest

The authors declare that they have no known competing financial interests or personal relationships that could have appeared to influence the work reported in this paper.

Acknowledgement

This study was supported by Istanbul Technical University Scientific Research Projects (ITU BAP, UAIP Projects) with the project number of MUA-2021-43196. The supercomputer resources for the computational part of this study have been provided by the National Center for High Performance Computing of Turkey (UHeM) under project number 4013952022.

REFERENCES

[1] Spear KE. Phase behavior and related properties of rare-earth borides. In: Phase diagrams. Elsevier; 1976. p. 91–159.
[2] Post B, Moskowitz D, Glaser FW. Borides of rare earth metals. J Am Chem Soc 1956;78:1800–2.
[3] Mori T. Novel physical properties of rare earth higher borides. J Phys Conf Ser 2009:176.
[4] Novikov VV, Pilipenko ES, Bud'ko SL. Crystal electric field effects and thermal expansion of rare-earth hexaborides. Solid State Commun 2017;252:51–3.
[5] Etourneau J, Hagenmuller P. Structure and physical features of the rare-earth borides. Philos Mag B Phys Condens Matter; Stat Mech Electron Opt Magn Prop 1985;52:589–610.
[6] Balakrishnan G, Lees M, Paul DM. Rare earth hexaborides: large single crystals. J Magn Magn Mater 2004;272–276:601–2.
[7] Stankiewicz J, Nakatsuji S, Fisk Z. Magnetotransport in Nd B6 single crystals. Phys Rev B Condens Matter 2005;71:1–6.
[8] Anisimova MA, Bogachb AV, Glushkova VV, Demishevb SV, Samarin NA, Filipovc VB, Shitsevalovac NY, Kuznetsovb AV, Sluchankob NE. Magnetoresistance and magnetic ordering in praseodymium and neodymium hexaborides. J Exp Theor Phys 2009;109:815–32.
[9] Ji XH, Zhang QY, Xu JQ, Zhao YM. Rare-earth hexaborides nanostructures: recent advances in materials, characterization and investigations of physical properties. Prog Solid State Chem 2011;39:51–69.
[10] Otani S, Nakagawa H, Nishi Y, Kieda N. Floating zone growth and high temperature hardness of rare-earth hexaboride crystals: LaB6, CeB6, PrB6, NdB6, and SmB6. J Solid State Chem 2000;154:238–41.
[11] Loewenhaupt M, Prager M. Crystal fields in PrB6 and NdB6. Z Phys B Condens Matter 1986;62:195–9.
[12] Liao PK, Spear KE, Schlesinger ME. The B-Nd (Boron-Neodymium) system. J Phase Equil 1996;17:335–9.
[13] Liu Y, Lu WJ, Qin JN, Zhang D. A new route for the synthesis of NdB6 powder from Nd2O3-B4C system. J Alloys Compd 2007;431:337–41.
[14] Sonber JK. Effect OF NdB_6 addition on densification and properties of ZrB_2. Ceram - Silikaty 2016:41–7.
[15] Xu J, Hou G, Mori T, Li H, Wang Y, Chang Y, Luo Y, Yu B, Ma Y, Zhai T. Excellent field-emission performances of neodymium hexaboride (NdB 6) nanoneedles with ultra-low work functions. Adv Funct Mater 2013;23:5038–48.
[16] Fink Z. The effect of crystal field splitings on the electrical resistivity OF NdB6. Solid State Commun 1976;18:221–3.
[17] Tamaki A, Goto T, Yoshizawa M, Fujimura T, K S, K T. Elastic softening and CEF effects OF NdB6 and PrB6. J Magn Magn Mater 1985;52:257–60.
[18] Vasil'ová M, Pristáš G, Reiffers M, Flachbart K, Rusz J, Shitsevalova N. Point-contact spectroscopy of crystalline electric field of heterocontacts PrB6 and NdB6 with Pt. Acta Phys Pol, A 2008;113:267–70.

[19] Reiffers M, Šebek J, Šantavá E, Shitsevalova N, Gabáni S, Pristáš G, Flachbart K. Heat capacity of NdB6. J Magn Magn Mater 2007;310:2006–8.
[20] Westrum EF, Andrews JTS, Justice BH, Justice BH, Johnson DA. Lanthanide hexaborides. I. Heat capacities and some thermophysical properties of LaB6, NdB6, and GdB6 at temperatures from 5 K to 350 K. J Chem Thermodyn 2002;34:239–50.
[21] McCarthy CM, Tompson CW. Magnetic structure of NdB6. J Phys Chem Solid 1980;41:1319–21.
[22] Goodrich RG, Harrison N, Fisk Z. Fermi surface changes across the nel phase boundary of NdB6. Phys Rev Lett 2006;97:1–4.
[23] Dou Z-H, Zhang T-A, Fan S-G, Huang Q-Y, Zhang J-L, Xiao H-Y, Fu N. A new method of preparing NdB6 ultra-fine powders. Rare Met; 2015.
[24] Simsek T, Avar B, Ozcan S, Kalkan B. Nano-sized neodymium hexaboride: room temperature mechanochemical synthesis. Phys B Condens Matter 2019;570:217–23.
[25] Han W, Zhang H, Chen J, Zhao Y, Fan Q, Li Q. Synthesis of single-crystalline NdB6 submicroawls via a simple flux-controlled self-catalyzed method. RSC Adv 2015;5:12605–12.
[26] Fan Q, Zhang Q, Zhao Y, Ding Q. Field emission from one-dimensional single-crystalline NdB6 nanowires. J Rare Earths 2013;31:145–8.
[27] Zhao X, Liu X, Lin F, Liu W, Su W. A new route for the synthesis of boron-rich rare-earth boride NdB6 under high pressure and high temperature. J Alloys Compd 1997;249:247–50.
[28] Zhou Y, Dai F, Xiang H, Liu B, Feng Z. Shear anisotropy: tuning high temperature metal hexaborides from soft to extremely hard. J Mater Sci Technol 2017;33:1371–7.
[29] Pan Y, Zheng WT, Guan WM, Zhang KH, Yu SS, Hu XY. Effect of boron vacancies on mechanical properties of ReB2 from first-principles calculation. Comput Mater Sci 2014;82:12–6.
[30] Balcı Ö, Ağaoğulları D, Öveçoğlu ML, Duman İ. Synthesis of niobium borides by powder metallurgy methods using Nb2O5, B2O3 and Mg blends. Trans Nonferrous Met Soc China (English Ed 2016;26:747–58.
[31] Ağaoğullari D, Duman I, Öveçoğlu ML. Synthesis of LaB 6 powders from La 2O 3, B 2O 3 and Mg blends via a mechanochemical route. Ceram Int 2012;38:6203–14.
[32] Ağaoğulları D, Balcı Ö, Akçamlı N, Suryanarayana C, Duman İ, Öveçoğlu M. Mechanochemical synthesis and consolidation of nanostructured cerium hexaboride. Process Appl Ceram 2019;13:32–43.
[33] Bale CW, Bélisle E, Chartrand P, Decterov SA, Eriksson G, Gheribi AE, Hack K, Jung IH, Kang YB, Melançon J, Pelton AD, Petersen S, Robelin C, Sangster J, Spencer P, Van Ende MA. FactSage thermochemical software and databases, 2010-2016. Calphad Comput Coupling Phase Diagrams Thermochem 2016;54:35–53.
[34] Suryanarayana C, Norton MG. X-ray diffraction: a practical approach. New York: Plenum Press; 1998.
[35] Perdew JP, Burke K, Ernzerhof M. Generalized gradient approximation made simple. 1996. p. 3865–8.
[36] Heyd J, Scuseria GE, Ernzerhof M, Heyd J, Scuseria GE, Ernzerhof M. Hybrid functionals based on a screened coulomb potential. 2003. p. 8207.
[37] Zhang SB, Northrup JE. Chemical potential dependence of defect formation energies in GaAs: application to Ga self-diff'usion67; 1991. p. 2339–42.
[38] Freysoldt C. Fully ab initio finite-size corrections for charged-defect supercell calculations. 2009. p. 1–4. 016402.
[39] Nazarov R, Hickel T, Neugebauer J. First-principles study of the thermodynamics of hydrogen-vacancy interaction in fcc iron. 2010. p. 1–11.
[40] Freysoldt C, Grabowski B, Hickel T, Neugebauer J, Kresse G, Janotti A, Walle CG, Van De. First-principles calculations for point defects in solids 2014;86:253–305.
[41] Parlinski K, Li ZQ, Kawazoe Y. First-principles determination of the soft mode in cubic ZrO 2 1997;4063:4063–6.
[42] Page Y Le, Saxe P. Symmetry-general least-squares extraction of elastic coefficients from ab initio total energy calculations 2001;63:1–8.
[43] Page Y Le, Saxe P. Symmetry-general least-squares extraction of elastic data for strained materials from ab initio calculations of stress 2002;65:1–14.
[44] Tan BT, Wu S, Anariba F, Wu P. A DFT study on brittle-to-ductile transition of d022-TiAl3 using multi-doping and strain-engineered effects. J Mater Sci Technol 2020;51:180–92.
[45] Chung DH, Buessem WR. The VoigtReussHill(VRH) approximation and the elastic moduli of polycrystalline ZnO , TiO2 (rutile), and Al2O3 the voigt-reuss-hill(VRH) approximation and the elastic moduli of polycrystalline, 2; 2013.
[46] Chen X, Niu H, Li D, Li Y. Intermetallics modeling hardness of polycrystalline materials and bulk metallic glasses. Intermetallics 2011;19:1275–81.
[47] ORSON L. ANDERSON. A simplified method for calculating the debye temperature from elastic constants24; 1963. p. 909–17.
[48] Bishop SR, Tuller HL, Kuru Y, Yildiz B. Chemical expansion of nonstoichiometric Pr0.1Ce0.9O2-δ: correlation with defect equilibrium model. J Eur Ceram Soc 2011;31:2351–6.
[49] Ma T, Jacobs R, Booske J, Morgan D. Work function trends and new low-work-function boride and nitride materials for electron emission applications. J Phys Chem C 2021;125:17400–10.
[50] Swanson LW, McNeely DR. Work functions of the (001) face of the hexaborides of Ba, La, Ce and Sm. Surf Sci 1979;83:11–28.
[51] Jiang Z, West D, Zhang S. A universal description of workfunction, 1–5; 2022.
[52] Gajdoš M, Hummer K, Kresse G, Furthmüller J, Bechstedt F. Linear optical properties in the projector-augmented wave methodology. Phys Rev B Condens Matter 2006;73:1–9.
[53] Moore EA, Smart LE. Optical properties of solids. Solid State Chem An Introd 2020;1269:283–314.
[54] Ağaoğullari D, Balci Ö, Öveçoğlu ML, Suryanarayana C, Duman I. Synthesis of bulk nanocrystalline samarium hexaboride. J Eur Ceram Soc 2015;35:4121–36.
[55] Suryanarayana C. Mechanical alloying and milling. Prog Mater Sci 2001;46(1–2):1–184.
[56] Xia Z, Guo S. Strain engineering of metal-based nanomaterials for energy electrocatalysis. Chem Soc Rev 2019;48:3265–78.
[57] Saito T, Saito T, Furuta T, Hwang J. Multifunctional alloys obtained via a dislocation-free plastic. 2014. p. 464.
[58] Souvatzis P, Katsnelson MI, Simak S, Ahuja R, Eriksson O. First-principles prediction of superplastic transition-metal alloys. 2004. p. 1–3. 012201.
[59] Senkov ON, Miracle DB. Generalization of intrinsic ductile-to-brittle criteria by Pugh and pettifor for materials with a cubic crystal structure. Sci Rep 2021;11:10–3.
[60] Han W, Zhao Y, Fan Q, Li Q. Preparation and growth mechanism of one-dimensional NdB6 nanostructures: nanobelts, nanoawls, and nanotubes. RSC Adv 2016;6:41891–6.